

Shiqu CHEN, Silei XIANG, Zehao TAN, Huiyuan LI, Xiaohui YAN, Jiewei YIN, Shuiyun SHEN, Junliang ZHANG

Exploration of the oxygen transport behavior in non-precious metal catalyst-based cathode catalyst layer for proton exchange membrane fuel cells

© Higher Education Press 2022

Abstract High cost has undoubtedly become the biggest obstacle to the commercialization of proton exchange membrane fuel cells (PEMFCs), in which Pt-based catalysts employed in the cathodic catalyst layer (CCL) account for the major portion of the cost. Although non-precious metal catalysts (NPMCs) show appreciable activity and stability in the oxygen reduction reaction (ORR), the performance of fuel cells based on NPMCs remains unsatisfactory compared to those using Pt-based CCL. Therefore, most studies on NPMC-based fuel cells focus on developing highly active catalysts rather than facilitating oxygen transport. In this work, the oxygen transport behavior in CCLs based on highly active Fe-N-C catalysts is comprehensively explored through the elaborate design of two types of membrane electrode structures, one containing low-Pt-based CCL and NPMC-based dummy catalyst layer (DCL) and the other containing only the NPMC-based CCL. Using Zn-N-C based DCLs of different thickness, the bulk oxygen transport resistance at the unit thickness in NPMC-based CCL was quantified via the limiting current method combined with linear fitting analysis. Then, the local and bulk resistances in NPMC-based CCLs were quantified via the limiting current method and scanning electron microscopy, respectively. Results show that the ratios of local and bulk oxygen transport resistances in NPMC-based CCL are 80% and 20%, respectively, and that an enhancement of local oxygen transport is critical to greatly

improve the performance of NPMC-based PEMFCs. Furthermore, the activity of active sites per unit in NPMC-based CCLs was determined to be lower than that in the Pt-based CCL, thus explaining worse cell performance of NPMC-based membrane electrode assemblies (MEAs). It is believed that the development of NPMC-based PEMFCs should proceed not only through the design of catalysts with higher activity but also through the improvement of oxygen transport in the CCL.

Keywords proton exchange membrane fuel cells (PEMFCs), non-precious metal catalyst (NPMC), cathode catalyst layer (CCL), local and bulk oxygen transport resistance

1 Introduction

Proton exchange membrane fuel cell (PEMFC) technology is considered the most attractive approach for the utilization of hydrogen as a fuel owing to its high efficiency, quietness, high reliability, and zero pollution. The use of hydrogen-fueled PEMFCs is expected to greatly promote the realization of the dual carbon goal, and thus they are receiving unprecedented attention in the automotive field. In addition to excellent performance, the cost should also be considered to meet the economic requirements of large-scale application [1]. Therefore, even though both the performance and lifetime of PEMFCs have already met and exceeded the requirements for large-scale application, their high cost owing to the use of expensive Pt-based catalysts is the main obstacle to commercialization. Furthermore, the cost of proton exchange membranes, gas diffusion layers, bipolar plates, and auxiliary components will be significantly reduced during mass production, but the cost of Pt-based catalysts is not expected to significantly

Received Jul. 13, 2022; accepted Sept. 23, 2022; online Nov. 20, 2022

Shiqu CHEN, Zehao TAN, Huiyuan LI, Xiaohui YAN, Jiewei YIN, Shuiyun SHEN (✉), Junliang ZHANG

Institute of Fuel Cells School of Mechanical Engineering, Shanghai Jiao Tong University, Shanghai 200240, China
E-mail: shuiyun_shen@sjtu.edu.cn

Silei XIANG
School of Vehicle and Mobility, State Key Laboratory of Automotive Safety and Energy, Tsinghua University, Beijing 100084, China

change. It has been predicted that the cost of Pt-based catalyst used in PEMFCs would account for about 41% of the cost of the entire fuel cell stack based on the stack cost breakdown for 500000 systems/year [2]. Additionally, the reaction kinetics of oxygen reduction reaction (ORR) is about five orders of magnitude slower than that of hydrogen oxidation reaction [3]; thus, Pt loading in the cathode is 6–10 times higher than that in the anode [4]. Therefore, the efforts on reducing Pt loading have been mainly focused on decreasing the amount of Pt for ORR in the cathode.

Accordingly, the development of low-cost non-precious metal catalysts (NPMCs) with high ORR activity and good stability (comparable to those of Pt) has become a research hotspot, and many appreciable performances have been reported [5–18]. Chang et al. [10] heat-treated a mixture of vitamin B12 and carbon black in a nitrogen environment at 700 °C to obtain a py-B12/C NPMC, which showed a half-wave potential of 0.78 V for the ORR in an acid environment. Wu et al. [11] developed a Fe-N-C catalyst using polyaniline as a precursor; this catalyst exhibited, as measured using rotating disk electrode (RDE), a half-wave potential of only 59 mV lower than that of commercial Pt/C catalyst and showed higher four-electron selectivity. Yin et al. [12] obtained a durable Co-N-C catalyst with a metal organic framework (MOF) structure, which showed a half-wave potential of 0.881 V in the RDE test and outstanding chemical and thermal stability: it resisted sintering at 900 °C. Yusuke et al. [13–16] studied the ORR catalytic performance of defect-rich graphene nanomesh, Fe-N-doped hollow carbon sphere-encapsulated iron carbide nanoparticles, Fe-N-doped porous carbon, and Mo₂C nanoparticles on N-doped carbon nanosheets and have achieved good performance. Shen et al. [19] prepared a durable Fe-N-C catalyst with MOF structure and carbon nanotubes, which showed the half-wave potential of 0.84 V in the RDE test. However, currently obtained M-N-C catalysts show much better ORR performance, especially stability, compared to commercial Pt/C catalysts. Zhang et al. [20] developed a membrane electrode assembly (MEA) with a MOF structure based on Fe-N-C; because of the Fenton's reaction caused by Fe and water flooding catalyst micropores that host most active sites of FeN_x, the performance dropped by 55% in the first 15 h of the durability test.

Although the ORR performance of NPMCs in the RDE tests is inspiring, further verification of their performance in fuel cell MEAs is still needed. Previous results on NPMC-based MEA are listed in Table 1. Wan et al. [22] reported a class of concave Fe-N-C single-atom catalysts with a peak power of 1180 mW/cm² at 0.47 V under 2.5 bar H₂-O₂ at 80 °C and 100% relative humidity (RH), which is the best performance reported thus far. This superior performance was ascribed to an enhanced

Table 1 Performance of recently reported NPMC-based MEAs

Catalyst type	Ref.	Catalyst loading/ (mg·cm ⁻²)	Pressure/ bar	Peak power density/ (mW·cm ⁻²)	Voltage/ V
PmPDA-GR-Fe	[21]	2.00	0.53	630	0.55
	[22]	2.00	2.50	1180	0.47
	[23]	3.00	2.00	900	0.45
	[24]	3.50	1.50	1100	0.40
	[25]	4.00	2.00	700	0.35
	[26]	4.00	1.40	860	0.39
	[27]	3.00	1.00	630	0.41
(Fe,Co)/N-C	[28]	0.77	1.50	850	0.40
Co-N-C	[29]	3.00	2.00	826	0.40
Mn-N-C	[30]	4.00	1.50	460	0.30

external surface area and mesoporosity, which exposed more inaccessible Fe-N₄ moieties and promoted oxygen transport in catalyst layers (CLs). Chen et al. [24] reported an MEA with 1100 mW/cm² peak power, measured under 1.5 bar H₂-O₂ at 80 °C and 100% RH, and a catalyst life of 20 h. They also designed experiments and density functional theory calculations to indicate that Fe at active sites of catalysts is attacked by hydroxyl free radicals formed by the decomposition of H₂O₂, and that the ionomer of the catalyst layer and the membrane are further contaminated by the leached Fe ions, which greatly affected the performance. Although the series of Fe-N-C catalysts have displayed similar catalytic activities to Pt, they rapidly degraded. In the previous study, Fe-N-C catalyst-based fuel cell exhibited an initial peak power density of 1100 mW/cm² but suffered a current loss of 52% over only 20 h at 0.4 V. On the one hand, Fe at active sites were attacked by hydroxyl free radicals formed by the decomposition of H₂O₂, and on the other hand, both the ionomer in CL and the membrane were contaminated by leached Fe ions. Several studies on NPMCs with metals such as Co and Mn have also been reported. It is believed that a high density of CoN₄ active sites not only results in higher power density but also leads to higher stability owing to their immunity to Fenton's reaction [26].

Although the RDE performance of NPMCs has been continuously improved, resulting in values closer and closer to that of Pt, there remains a big gap in the fuel cell performance, especially in the high current density region. NPMC-based cathodic catalyst layers (CCLs) usually have at least 10 times greater thickness than Pt-based CCLs. It is speculated that the improvement in cell performance for real applications, in addition to the development of highly active and durable NPMCs, also requires the enhancement of oxygen transport in the CCL. However, oxygen transport in the NPMC-based CCLs remains unexplored; thus, a more solid theoretical background is needed to guide the structural design of

CCLs. Usually, oxygen transport in the CCL can be divided into bulk oxygen transport and local oxygen transport. The bulk oxygen transport resistance refers to the resistance caused by the molecular diffusion and Knudsen diffusion of oxygen in microporous structures of CCL [31], and the local oxygen transport resistance is the resistance to the passage of oxygen through ultrathin Nafion film on the catalyst surface [32]. In Pt-based CCLs, the roles of bulk and local diffusion in the CCL change as the Pt loading decreases. In high-Pt-based MEAs, the transfer resistance is mainly bulk oxygen transport resistance, whereas in low-Pt-based MEAs, local oxygen transport resistance dominates. Nonoyama et al. [33] researched the contributions of molecular and Knudsen diffusion and determined the permeation through the ionomer film covering the catalyst-layer agglomerates; they concluded that the ionomer-film resistance is dominant, especially at lower temperatures and Pt loadings. Schuler et al. [34] used operando method based on H₂ limiting current to study Pt-based MEAs and found that the local oxygen transport resistance through the ionomer thin film or very local to the reaction site dominates (accounts for 60%–80%) in low-Pt-based MEAs with loadings from 0.03 to 0.1 mg/cm². It has also been proven that along with the decrease in Pt loading from 0.2 to 0.05 mg/cm², the proportion of local oxygen transport resistance increases from 44% to 77% [35].

However, thus far, few studies focused on the oxygen transport resistance in the NPMC-based CCL, especially on a quantitative relationship between bulk and local oxygen transport resistance. Herein, we comprehensively explored the oxygen transport behavior in a Fe-N-C catalyst-based CCL via the limiting current method combined with mathematical derivation testing. More importantly, a homemade MOF structured Fe-N-C catalyst with a good ORR activity (half-wave potential of 0.84 V [19]) was employed to prepare CCLs. An MEA with low-Pt-based CCL and NPMC-based dummy catalyst layer (DCL) and MEA with NPMC-based CCL were designed to quantitatively analyze bulk and local oxygen transport resistance in the NPMC-based CCL. DCL had the same structure as CCL but without catalytic activity; thus, its oxygen transport resistance consisted only of bulk oxygen transport resistance. The obtained results suggest that although the thickness of the NPMC-based CCL is larger than that of the Pt-based CCL, the bulk oxygen transport resistance in the NPMC-based CCL accounts for only about 20% of oxygen transport resistance in CCL. The related reasons are speculated below.

The novelty of this study is that the bulk and local oxygen transport resistances in NPMC-based CCLs were quantitatively analyzed using the limiting current method combined with mathematical models based on two MEA structures designed specifically for NPMCs, which fills the gap in the research on oxygen transport resistance in NPMC-based CCLs.

2 Experimental section

2.1 Chemicals and materials

Methanol (CH₃OH, 99%, Sinopharm Chemical Reagent), 2-methylimidazole (98%, Sigma-Aldrich), zinc nitrate hexahydrate (Zn(NO₃)₂·6H₂O, 99%, Sigma-Aldrich), ferric nitrate nonahydrate (Fe(NO₃)₃·9H₂O, 99%, Sigma-Aldrich), Nafion solution (D2021, 20% (mass fraction), Dupont), ethanol (C₂H₅OH, 99.7%, Sinopharm Chemical Reagent), isopropyl alcohol (C₃H₈O, 99.7%, Sinopharm Chemical Reagent), 10 direct flow channel (0.5 mm × 0.5 mm × 0.8 mm), gas diffusion layer (GDS3250, Ballard), Pt/C catalyst (TEC10V50E, TANAKA), proton exchange membrane (Nafion 211, Dupont), centrifuge tube (10 mL, CORNING), and ultrapure water (> 18.2 MΩ·cm, Millipore) were used in this study.

2.2 Physicochemical characterizations

Scanning electron microscopy (SEM; Mira3 type, Czech TESCAN, 5 kV) was used to characterize the micromorphology of sample surfaces [36] to measure the thickness of CLs and examine the particle morphology and pore distribution in CLs. Before SEM, liquid nitrogen quenching was performed to obtain a clean and undamaged section. To ensure that the sample cross-section was slightly higher than the surface of the SEM sample stage, the sample was mounted on conductive glue.

2.3 Electrochemical measurements

Fuel cell test bench (C10-LT mit EIS CYV V002, Fuelcon) was used to perform the tests. During the test, the cathode was fed with a mixture of oxygen and nitrogen; the anode was fed with hydrogen; the reaction temperature was maintained at 80°C; the humidity at the cathode and anode was 67% RH; cathode and anode reaction gas pressure was 151 kPa_{abs}; water pressure in the channel was 31.3 kPa_{abs}; and flow rates at the anode and cathode were maintained at 0.8 and 1.5 L/min, respectively. The limiting current was determined using linear sweep voltammetry with the sweep range from open circuit voltage to 0.05 V at the sweep rate of 5 mV/s.

3 Results and discussion

3.1 Analysis of local and bulk oxygen transport resistance

To separate the bulk and local oxygen transport resistance in the Pt-based CCL, one layer of DCL was sprayed onto the CCL [35]. At the same time, NPMCs usually have insufficient activity to reach the limiting current; thus, an additional layer of Pt-based CCL was added to assist in

calculating the bulk resistance of the NPMC-based CCL. Additionally, it was noted that the NPMC-based CCL is much thicker than the Pt-based CCL, which may lead to a larger bulk oxygen transport resistance. Figure 1(a) presents schematics of the MEA with one layer of Pt-based CCL and one layer of Zn-N-C-based DCL.

The Zn-N-C DCL was synthesized in the same way as the Fe-N-C catalyst but without adding Fe precursors. This ensured that the DCL contained no active sites but possessed the same material and layer structures as the CCL. Thus, in DCL, there was no local oxygen transport resistance but only bulk oxygen transport resistance. If the thickness of DCL is much larger than that of the Pt-based CCL, the bulk oxygen transport resistance in DCL will be much higher than that in Pt-based CCL. The total oxygen transport resistance can be expressed by the following equation:

$$R_{\text{total}} = R_{\text{channel}} + R_{\text{GDL}} + r_{\text{bulk,DCL}} \times \delta_{\text{DCL}} + R_{\text{local,CCL}} \quad (\delta_{\text{DCL}} \gg \delta_{\text{CCL}}), \quad (1)$$

where R_{total} is the total oxygen transport resistance, R_{channel} and R_{GDL} are the oxygen transport resistances of flow channel and gas diffusion layer, respectively, and δ_{DCL} and δ_{CCL} are the thicknesses of the DCL and CCL, respectively.

R_{total} was obtained using the limiting current method. When approaching the limiting current, the oxygen concentration on the catalyst surface is 0. By combining Faraday's law, Fick's first law, and the ideal gas state equation, the following calculation equation can be easily obtained [35]:

$$R_{\text{total}} = 4F \times \frac{c_{O_2}^{\text{channel}}}{i_{\text{lim}}} = \frac{4F x_{O_2} p_{\text{channel}}}{RT} \times \frac{1}{i_{\text{lim}}}, \quad (2)$$

where $c_{O_2}^{\text{channel}}$ is the channel oxygen concentration, i_{lim} is the limiting current density, x_{O_2} is the mole fraction of oxygen, p_{channel} is the channel pressure, R is the gas constant, and T is the reaction temperature.

Combining Eq. (1) and Eq. (2) gives the following equation:

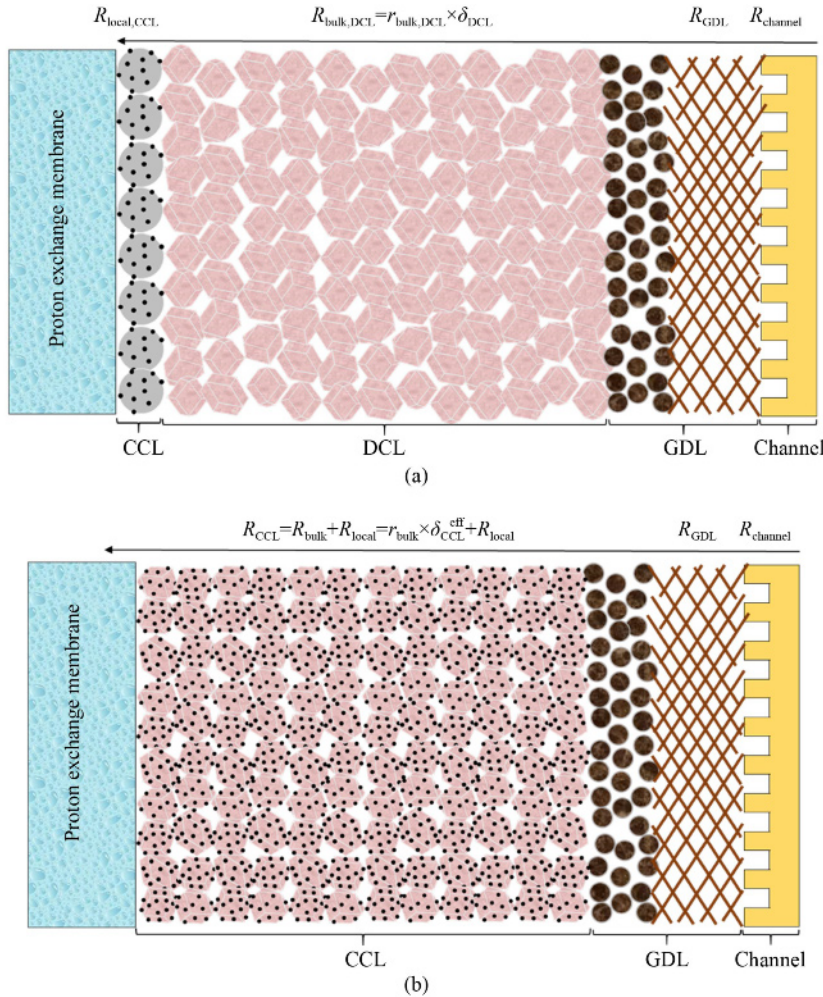


Fig. 1 Schematic of MEA.

(a) MEA with Pt-based CCL and Zn-N-C-based DCL; (b) MEA with NPMC-based CCL and without DCL.

$$\frac{1}{i_{\text{lim}}} = \frac{RT}{4F x_{O_2} p_{\text{channel}}} r_{\text{bulk,DCL}} \times \delta_{\text{DCL}} + RT \frac{(R_{\text{channel}} + R_{\text{GDL}} + R_{\text{local,CCL}})}{4F x_{O_2} p_{\text{channel}}}. \quad (3)$$

The consumption of oxygen during transport may be calculated using the following equation [37]:

$$R_{\text{CCL}} = R_{\text{bulk}} + R_{\text{local}} = r_{\text{bulk}} \times \delta_{\text{CCL}}^{\text{eff}} + R_{\text{local}}, \quad (4)$$

where $\delta_{\text{CCL}}^{\text{eff}}$ is ca. one-third of the CCL thickness (δ_{CCL}). It was thus concluded that there exists a linear relationship between the reciprocal of limiting current and the thickness of DCL.

First, using δ_{DCL} as the independent variable in the experiment, the limiting currents of DCLs with different thicknesses were experimentally obtained. The unit bulk oxygen transport resistance of DCL, which is the same as that of NPMC-based CCL, was obtained by fitting the slope. The local oxygen transport resistance of the Pt-based CCL was obtained from the intercept. Second, as shown in Fig. 1(b), the NPMC-based MEA without DCL was prepared, and the total resistance in CCL was measured. Then, the local oxygen transport resistance in NPMC-based CCL was calculated.

3.2 Experimental results and discussion for MEA with Zn-N-C DCL

The limiting current measurements were performed at 1%, 4%, 8%, 21%, and 99% oxygen concentrations. Figure 3 shows the corresponding polarization curves at

different oxygen concentrations. All the polarization curves contain the concentration polarization control zone, especially the polarization curves at oxygen concentrations of 1% and 4%. Considering that the subsequent reduction in the DCL thickness according to the gradient change may lead to better oxygen transport performance, the limiting current cannot be measured at 4% oxygen concentration. To ensure that the concentration polarization control zone always occurs with the decrease in DCL thickness, subsequent measurements of limiting current were conducted at 1% oxygen concentration.

Figure 4 presents the limiting currents of MEA structures with different DCL thicknesses at 1% oxygen concentration. Labels DCL1–4 represent DCL thicknesses from small to large (determined by SEM) in MEA with Pt-based CCL and Zn-N-C DCL. The experimental results confirmed that a greater thickness of DCL leads to a higher oxygen transport resistance, and according to Eq. (2), to lower limiting current density.

Figure 5 shows representative SEM images of DCLs with different thicknesses. The SEM results show that the thickness of DCL can be measured very accurately, and the thicknesses of DCL and proton exchange membrane are much greater than that of Pt-based CCL, making it difficult to determine the thickness of the Pt-based CCL in SEM images of MEAs with DCL. Therefore, SEM characterizations of the Pt-based CCL were performed independently. Results indicate that the thickness of the Pt-based CCL is much smaller than that of DCL, which

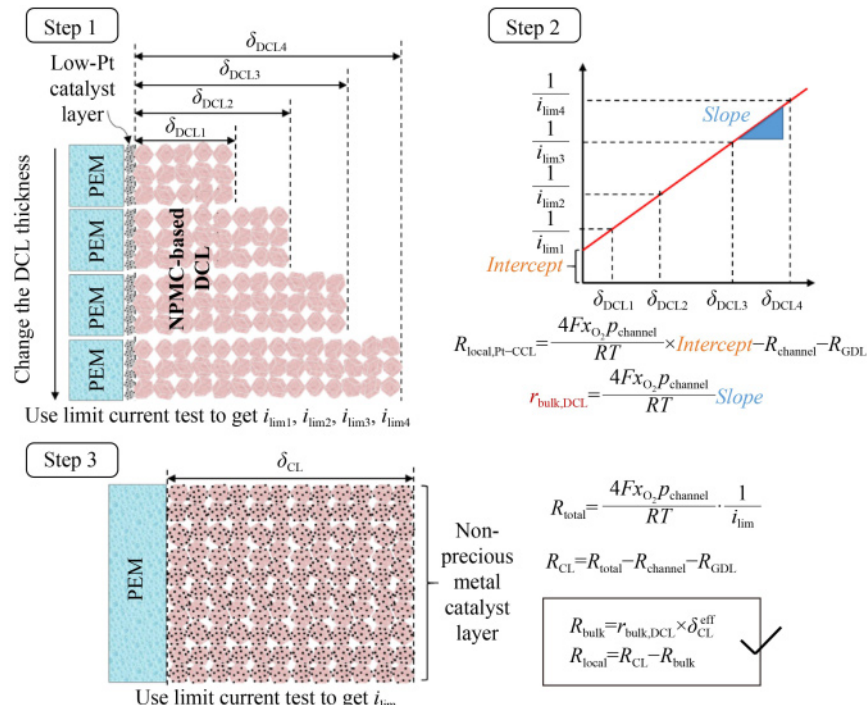


Fig. 2 Introduction to the experimental method used to determine local and bulk oxygen transport resistance.

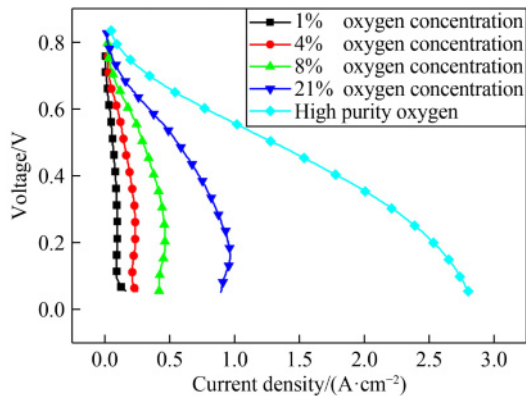


Fig. 3 Limiting current test of MEA with Pt-based CCL and Zn-N-C DCL.

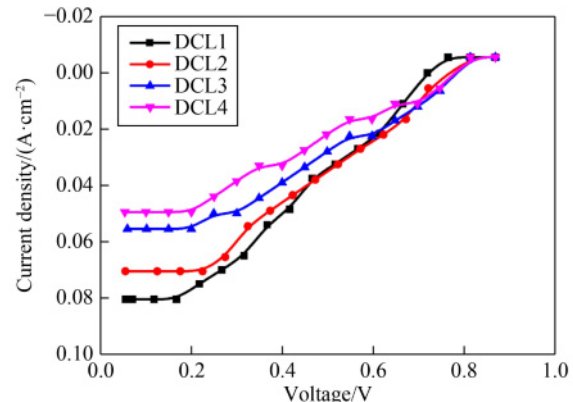


Fig. 4 Limiting current test results for MEAs with different DCL thicknesses.

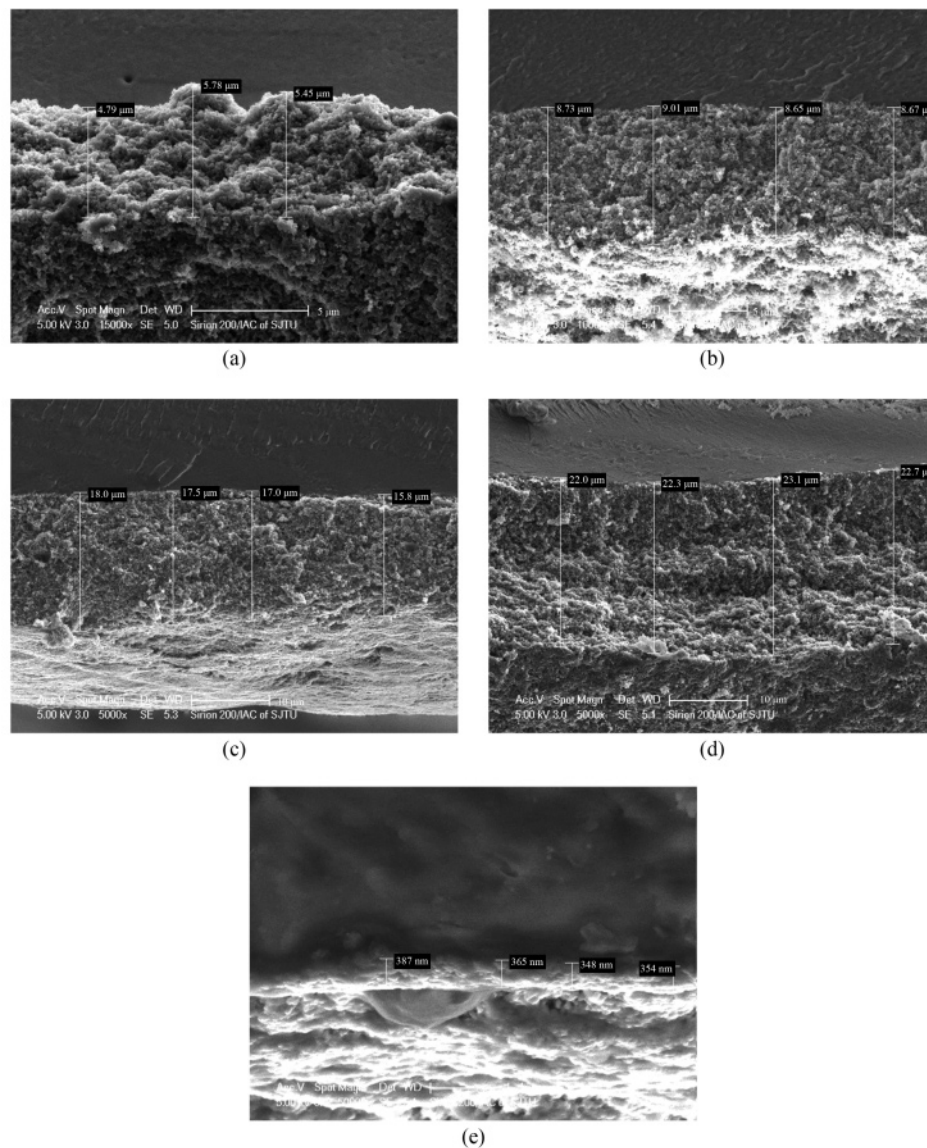


Fig. 5 SEM images for accurate thickness measurement.
(a) DCL1; (b) DCL2; (c) DCL3; (d) DCL4; (e) Pt-based CCL.

confirms the experimental hypothesis.

Table 2 summarizes the above electrochemical tests and SEM characterization results. **Figure 6** illustrates the relationship between $1/i_{\text{lim}}$ and DCL thickness.

The slope obtained by fitting is $0.453 \times 10^4 \text{ cm}/\text{A}$, and the intercept is $10.133 \text{ cm}^2/\text{A}$. Therefore, $r_{\text{bulk,DCL}}$ can be calculated using Eq. (5):

$$r_{\text{bulk,DCL}} = \frac{4FO_2P_{\text{channel}}}{RT} \times \text{Slope} = 711.9 \text{ s/cm}^2. \quad (5)$$

The r_{bulk} of the NPMC-based MEA is nearly half of the r_{bulk} of Pt-based MEA (1800 s/cm^2). Surprisingly, the bulk oxygen transport behavior in NPMC-based CCL is better than that in Pt-based CCL under the condition of unit thickness, although the thickness of the entire CCL needs to be considered to determine the overall bulk oxygen transport.

3.3 Experimental results and discussion for MEA without DCL

Optimal loading of 5.28 mg/cm^2 Fe-N-C catalyst was used to prepare the NPMC-based CCL, the peak power of which reached 553.65 mW/cm^2 ; the optimization is shown in **Fig. 7**. The limiting current test was performed at 1% and 4% oxygen concentrations, and the corresponding test results are shown in **Fig. 8**.

The total oxygen transport resistances at two oxygen concentrations were calculated according to Eq. (2), and

Table 2 Data summary of electrochemical tests and SEM characterization results

Sample	DCL thickness/ μm	Standard deviation of DCL thickness	$i_{\text{lim}}/(\text{A}\cdot\text{cm}^{-2})$	Standard deviation of i_{lim}	$1/i_{\text{lim}}/(\text{cm}^2\cdot\text{A}^{-1})$
DCL1	5.39	0.376	0.080	0.00113	12.500
DCL2	8.85	0.257	0.071	0.00185	14.164
DCL3	17.08	0.943	0.055	0.00082	18.293
DCL4	22.53	0.479	0.049	0.00155	20.228

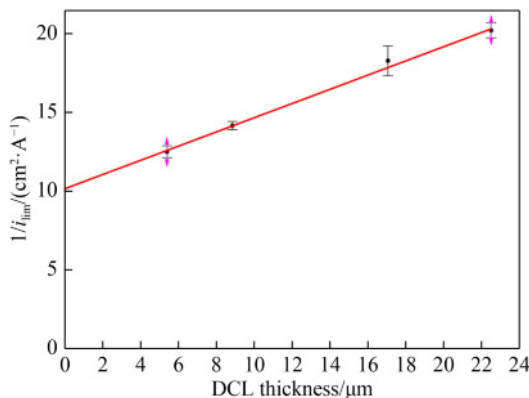


Fig. 6 Plot of Eq. (3), which illustrates the relationship between $1/i_{\text{lim}}$ and DCL thickness.

their average comprised

$$R_{\text{total}} = 7.538 \text{ s/cm}. \quad (6)$$

Figure 9 shows the SEM image of the NPMC-based MEA with optimal loading. In this way, the thickness of CCL could be accurately measured.

Baker et al. [38] have previously studied oxygen transport in channels and gave an empirical equation for R_{channel} :

$$R_{\text{channel}} = A \frac{a}{D_{O_2}^{\text{CH}}} + B \frac{2NdL}{Q_{\text{dry}}} \left(\frac{273}{T} \right) \frac{P - P_w}{P_0}, \quad (7)$$

where A and B are two empirical parameters related to the size of the flow channel, which were obtained from the literature; a , d , L , and N are the size parameters of the flow field; half the width of the flow field, depth, length, and the number of flow channels, respectively; $D_{O_2}^{\text{CH}}$ is the oxygen diffusion coefficient in the flow channel; P , P_0 , and P_w are the gas pressure in the flow channel, atmospheric pressure, and water vapor partial pressure, respectively; Q_{dry} is the total gas flow, and T is the temperature of the MEA.

The parameters were plugged into Eq. (7), yielding $R_{\text{channel}} = 0.26 \text{ s/cm}$. The gas diffusion layer used in this study was GDS3250 carbon with $R_{\text{channel}} = 0.14 \text{ s/cm}$ [35]; thus, the local and bulk oxygen transport resistances in the NPMC-based CCL are

$$R_{\text{CCL}} = R_{\text{total}} - R_{\text{channel}} - R_{\text{GDL}} = 7.138 \text{ s/cm},$$

$$R_{\text{bulk}} = r_{\text{bulk,DCL}} \times \delta_{\text{CCL}}^{\text{eff}} = 1.438 \text{ s/cm},$$

$$R_{\text{local}} = R_{\text{CCL}} - R_{\text{bulk}} = 5.700 \text{ s/cm}.$$

It is thus concluded that the oxygen transport resistance in the NPMC-based CCL is much greater than that in the Pt-based CCL. In NPMC-based CCL, the local oxygen transport resistance is larger than bulk oxygen transport resistance, accounting for nearly 80% of the total oxygen transport resistance of the CCL. In the Pt-based CCL, the proportion of local oxygen transport resistance increases with decreasing Pt loading, with the local oxygen transport resistance accounting for 77% of the total oxygen transport resistance in the low-Pt-based CCL [35]. The local oxygen transport resistance in Pt-based CCLs occurs during the transport of oxygen through the Nafion phase on the catalyst surface to Pt active sites. The following points may explain the reasons for the differences:

1) Probably because of the better molecular and Knudsen diffusion of oxygen in the microporous structure of the NPMC-based CCL, the r_{bulk} in the NPMC-based CCL is better than that in the Pt-based CCL [31, 39]. However, the thickness of the NPMC-based CCL is an order of magnitude higher than that of the Pt-based CCL; hence, it can be shown that the R_{bulk} in the NPMC-based CCL is larger than that in the Pt-based CCL. NPMCs have lower activity than Pt/C catalysts;

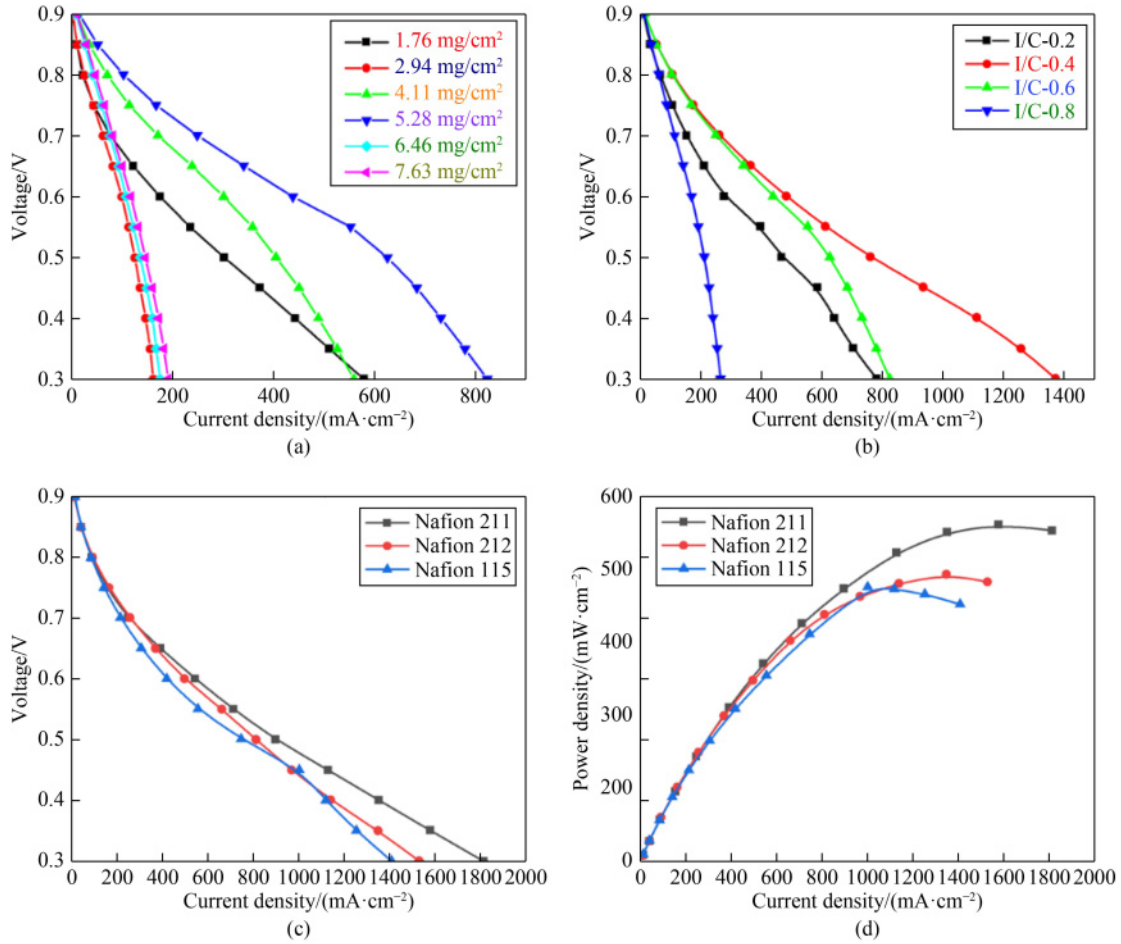


Fig. 7 Polarization curves and peak power densities of MEA optimization.

(a) Polarization curves of MEAs with different NPMC loadings; (b) polarization curves of MEAs with different I/C; (c) polarization curves of MEAs with different proton exchange membranes; (d) peak power densities of MEAs with different proton exchange membranes.

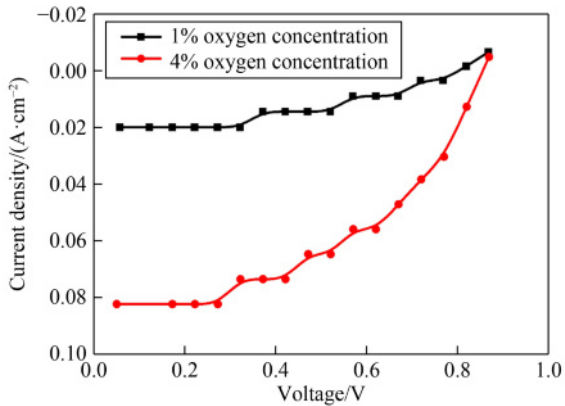


Fig. 8 MEA with optimal loading tested at 1% and 4% oxygen concentrations.

therefore, to attain similar catalytic activity of the MEA, a higher loading of the NPMC-based CCL is required, resulting in a much larger thickness compared to the Pt-based CCL MEA, leading to a greater bulk oxygen transport resistance.

2) Although it was expected that a larger thickness of CCL would lead to more active sites in the CCL and consequently smaller local oxygen transport resistance, the obtained results show that its absolute value is larger than that in the Pt-based CCL. This, to a certain extent, indicates that in the NPMC-based CCL under unit loading, there are fewer active sites than that in the Pt-based CCL, which is also one of the important reasons for the lower performance of the NPMC-based MEA compared to the Pt-based MEA.

3) It is also concluded that the absolute values of bulk or local oxygen transport resistance in NPMC-based CCL are greater than those in the Pt-based CCL. Considering the larger proportion of local mass transfer resistance, it is very important to further increase the number of active sites in the NPMC-based CCL per unit thickness. For the same huge bulk oxygen transport resistance, in future studies, the NPMC-based CCL could be further modified using pore-forming agents to increase the specific surface area or using templates to produce porous structures [40], thereby improving its oxygen transport performance.

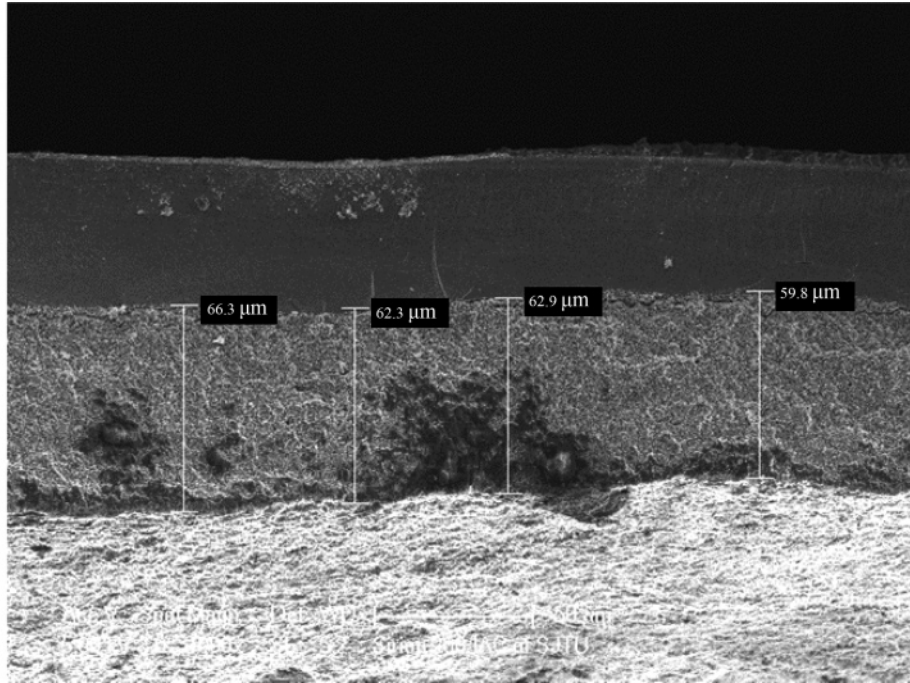


Fig. 9 SEM image of the NPMC-based MEA with optimal loading.

4 Conclusions

Because of the low cost and promising ORR activity of NPMCs, their use is expected to ultimately help solve the issue of high cost of fuel cells. Most current studies in this field focus on improving activity; therefore, the effect of oxygen transport in the NPMC-based MEAs remains to be clarified for practical applications. The thickness of NPMC-based CCLs is much larger than that of Pt-based CCLs, which inevitably causes larger oxygen transport resistance. In this work, two types of MEA structures, with and without DCL, were designed to efficiently quantify the impact of bulk and local oxygen transport resistances in the NPMC-based CCL on cell performance, which is expected to guide further optimization of cell performance of NPMC-based PEMFCs. Some enlightening conclusions for further enhancing the performance of NPMC-based PEMFCs are presented below:

1) Studies on oxygen transport in NPMC-based MEAs should focus on CCLs. The effect of local oxygen transport resistance on cell performance is greater than that of bulk oxygen transport resistance in NPMC-based CCLs, accounting for nearly 80% of total oxygen transport resistance.

2) Probably because of the better molecular and Knudsen diffusion of oxygen in the microporous structure of the NPMC-based CCL, the r_{bulk} in the NPMC-based CCL is better than that in the Pt-based CCL. However, NPMC-based CCLs are usually an order of magnitude thicker than Pt-based CCLs; thus, the

absolute value of r_{bulk} in the former is higher.

3) A greater thickness of CCLs promises more active sites, leading to a smaller local oxygen transport resistance. However, in NPMC-based CCLs, its absolute value remains high because of the lower activity of active sites per unit than that in Pt-based CCLs, thus decreasing the cell performance of NPMC-based MEAs.

Acknowledgments The work was financially supported by the National Key R&D Program of China (Grant No. 2021YFB4001303) and the National Natural Science Foundation of China (Grant No. 21975157). We also want to thank Dr. Jiewei Yin for the guidance on fuel cell tests for this study.

Electronic Supplementary Material Supplementary material is available in the online version of this article at <https://doi.org/10.1007/s11708-022-0849-1> and is accessible for authorized users.

Notations

A	Empirical parameter A
a	Half the width of the flow field
B	Empirical parameter B
$c_{\text{O}_2}^{\text{channel}}$	Concentration of oxygen in flow channel
d	Depth of flow channel
$217D_{\text{O}_2}^{\text{CH}}$	Oxygen diffusion coefficient in flow channel
F	Faraday's constant
i_{lim}	Limiting current density
L	Length of flow channel

<i>N</i>	Number of flow channel
<i>P</i>	Gas pressure in flow channel
<i>P</i> ₀	Atmospheric pressure
<i>P</i> _{channel}	Flow channel pressure
<i>P</i> _w	Water vapor partial pressure
<i>Q</i> _{dry}	Total gas flow
<i>R</i>	gas constant
<i>r</i> _{bulk,DCL}	Bulk oxygen transport resistance of DCL per unit thickness
<i>R</i> _{local,CCL}	Local oxygen transport resistance of CCL
<i>R</i> _{channel}	Oxygen transport resistance of flow channel
<i>R</i> _{CCL}	Oxygen transport resistance of CCL
<i>R</i> _{GDL}	Oxygen transport resistance of gas diffusion layer
<i>R</i> _{total}	Total oxygen transport resistance
<i>Slope</i>	Fitted curve slope
<i>T</i>	Reaction temperature
<i>x</i> _{O₂}	Mole fraction of oxygen
<i>δ</i> _{CCL}	Thickness of CCL
<i>δ</i> _{CCL} ^{eff}	Effective thickness of CCL
<i>δ</i> _{DCL}	Thickness of DCL

References

1. Liu S, Kang L, Jun S C. Challenges and strategies toward cathode materials for rechargeable potassium-ion batteries. *Advanced Materials*, 2021, 33(47): 2004689
2. Luo X, Guo Y, Zhou H, et al. Thermal annealing synthesis of double-shell truncated octahedral Pt-Ni alloys for oxygen reduction reaction of polymer electrolyte membrane fuel cells. *Frontiers in Energy*, 2020, 14(4): 767–777
3. Shao M, Chang Q, Dodelet J P, et al. Recent advances in electrocatalysts for oxygen reduction reaction. *Chemical Reviews*, 2016, 116(6): 3594–3657
4. Kongkanand A, Mathias M F. The priority and challenge of high-power performance of low-platinum proton-exchange membrane fuel cells. *Journal of Physical Chemistry Letters*, 2016, 7(7): 1127–1137
5. Xue J, Li Y, Hu J. Nanoporous bimetallic Zn/Fe-N-C for efficient oxygen reduction in acidic and alkaline media. *Journal of Materials Chemistry. A, Materials for Energy and Sustainability*, 2020, 8(15): 7145–7157
6. Chao Y, Tsai D, Wu A, et al. Cobalt selenide electrocatalyst supported by nitrogen-doped carbon and its stable activity toward oxygen reduction reaction. *International Journal of Hydrogen Energy*, 2013, 38(14): 5655–5664
7. Jing S, Luo L, Yin S, et al. Tungsten nitride decorated carbon nanotubes hybrid as efficient catalyst supports for oxygen reduction reaction. *Applied Catalysis B: Environmental*, 2014, 147: 897–903
8. Ishihara A, Lee K, Doi S, et al. Tantalum oxynitride for a novel cathode of PEFC. *Electrochemical and Solid-State Letters*, 2005, 8(4): A201
9. Li L, Fu C, Shen S, et al. Influence of Fe on electrocatalytic activity of iron-nitrogen-doped carbon materials toward oxygen reduction reaction. *Frontiers in Energy*, 2020, <https://doi.org/10.1007/s11708-020-0669-0>
10. Li L, Shen S, Li X, et al. A derivative of mesoporous oxygen reduction reaction electrocatalysts from citric acid and dicyandiamide. *International Journal of Hydrogen Energy*, 2020, 45(11): 6563–6572
11. Wu G, More K L, Johnston C M, et al. High-performance electrocatalysts for oxygen reduction derived from polyaniline, iron, and cobalt. *Science*, 2011, 332(6028): 443–447
12. Yin P, Yao T, Wu Y, et al. Single cobalt atoms with precise N-coordination as superior oxygen reduction reaction catalysts. *Angewandte Chemie International Edition*, 2016, 55(36): 10800–10805
13. Xia W, Tang J, Li J, et al. Defect-rich graphene nanomesh produced by thermal exfoliation of metal–organic frameworks for the oxygen reduction reaction. *Angewandte Chemie*, 2019, 131(38): 13488–13493
14. Tan H, Li Y, Kim J, et al. Sub-50 nm iron–nitrogen-doped hollow carbon sphere-encapsulated iron carbide nanoparticles as efficient oxygen reduction catalysts. *Advancement of Science*, 2018, 5(7): 1800120
15. Tan H, Tang J, Henzie J, et al. Assembly of hollow carbon nanospheres on graphene nanosheets and creation of iron–nitrogen-doped porous carbon for oxygen reduction. *ACS Nano*, 2018, 12(6): 5674–5683
16. Guo Y, Tang J, Henzie J, et al. Assembly of hollow mesoporous nanoarchitectures composed of ultrafine Mo₂C nanoparticles on N-doped carbon nanosheets for efficient electrocatalytic reduction of oxygen. *Materials Horizons*, 2017, 4(6): 1171–1177
17. Shen H, Jiang H, Liu Y, et al. Cobalt@cobalt carbide supported on nitrogen and sulfur co-doped carbon: an efficient non-precious metal electrocatalyst for oxygen reduction reaction. *Acta Physico-Chimica Sinica*, 2017, 33(9): 1811–1821
18. Wang Q, Liu D, He X. Metal-organic framework-derived Fe-N-C nanohybrids as highly-efficient oxygen reduction catalysts. *Acta Physico-Chimica Sinica*, 2019, 35(7): 740–748
19. Shen S, Ren Z, Xiang S, et al. The development of a highly durable Fe-N-C electrocatalyst with favorable CNT structures for the oxygen reduction in PEMFCs. *Journal of Electrochemical Energy Conversion and Storage*, 2022, 19(1): 010905
20. Zhang G, Chenitz R, Lefèvre M, et al. Is iron involved in the lack of stability of Fe/N/C electrocatalysts used to reduce oxygen at the cathode of PEM fuel cells? *Nano Energy*, 2016, 29: 111–125
21. Wang T, Wang J, Wang X, et al. Graphene-templated synthesis of sandwich-like porous carbon nanosheets for efficient oxygen reduction reaction in both alkaline and acidic media. *Science China Materials*, 2018, 61(7): 915–925 (in Chinese)
22. Wan X, Liu X, Li Y, et al. Fe-N-C electrocatalyst with dense active sites and efficient mass transport for high-performance proton exchange membrane fuel cells. *Nature Catalysis*, 2019, 2(3): 259–268
23. Shui J, Chen C, Grabstanowicz L, et al. Highly efficient nonprecious metal catalyst prepared with metal–organic framework in a continuous carbon nanofibrous network. *Proceedings of the National Academy of Sciences of the United*

- States of America, 2015, 112(34): 10629–10634
- 24. Chen J, Yan X, Fu C, et al. Insight into the rapid degradation behavior of nonprecious metal Fe-N-C electrocatalyst-based proton exchange membrane fuel cells. *ACS Applied Materials & Interfaces*, 2019, 11(41): 37779–37786
 - 25. Zhang N, Zhou T, Chen M, et al. High-purity pyrrole-type FeN₄ sites as a superior oxygen reduction electrocatalyst. *Energy & Environmental Science*, 2020, 13(1): 111–118
 - 26. Fu X, Li N, Ren B, et al. Tailoring FeN₄ sites with edge enrichment for boosted oxygen reduction performance in proton exchange membrane fuel cell. *Advanced Energy Materials*, 2019, 9(11): 1803737
 - 27. Zhan Y, Zeng H, Xie F, et al. Templated growth of Fe/N/C catalyst on hierarchically porous carbon for oxygen reduction reaction in proton exchange membrane fuel cells. *Journal of Power Sources*, 2019, 431: 31–39
 - 28. Wang J, Huang Z, Liu W, et al. Design of N-coordinated dual-metal sites: a stable and active Pt-free catalyst for acidic oxygen reduction reaction. *Journal of the American Chemical Society*, 2017, 139(48): 17281–17284
 - 29. Chen L, Liu X, Zheng L, et al. Insights into the role of active site density in the fuel cell performance of Co-N-C catalysts. *Applied Catalysis B: Environmental*, 2019, 256: 117849
 - 30. Li J, Chen M, Cullen D A, et al. Atomically dispersed manganese catalysts for oxygen reduction in proton-exchange membrane fuel cells. *Nature Catalysis*, 2018, 1(12): 935–945
 - 31. Owejan J P, Owejan J E, Gu W, et al. Water transport mechanisms in PEMFC gas diffusion layers. *Journal of the Electrochemical Society*, 2010, 157(10): 1456–1464
 - 32. Perry M L, Newman J, Cairns E J. Mass transport in gas-diffusion electrodes: a diagnostic tool for fuel-cell cathodes. *Journal of the Electrochemical Society*, 1998, 145(1): 5–15
 - 33. Nonoyama N, Okazaki S, Weber A Z, et al. Analysis of oxygen-transport diffusion resistance in proton-exchange-membrane fuel cells. *Journal of the Electrochemical Society*, 2011, 158(4): B416
 - 34. Schuler T, Chowdhury A, Freiberg A T, et al. Fuel-cell catalyst-layer resistance via hydrogen limiting-current measurements. *Journal of the Electrochemical Society*, 2019, 166(7): F3020–F3031
 - 35. Wang C, Cheng X, Lu J, et al. The experimental measurement of local and bulk oxygen transport resistances in the catalyst layer of proton exchange membrane fuel cells. *Journal of Physical Chemistry Letters*, 2017, 8(23): 5848–5852
 - 36. Kang L, Wang X, Liu S, et al. Bio-inspired interface engineering of Ag₂O rooted on Au, Ni-modified filter paper for highly robust Zn–Ag₂O batteries. *Journal of Colloid and Interface Science*, 2022, 623: 744–751
 - 37. Ono Y, Ohma A, Shinohara K, et al. Influence of equivalent weight of ionomer on local oxygen transport resistance in cathode catalyst layers. *Journal of the Electrochemical Society*, 2013, 160(8): 779–787
 - 38. Baker D R, Caulk D A, Neyerlin K C, et al. Measurement of oxygen transport resistance in PEM fuel cells by limiting current methods. *Journal of the Electrochemical Society*, 2009, 156(9): 991–1003
 - 39. Cheng X, Wei G, Wang C, et al. Experimental probing of effects of carbon support on bulk and local oxygen transport resistance in ultra-low Pt PEMFCs. *International Journal of Heat and Mass Transfer*, 2021, 164: 120549
 - 40. Liu S, Kang L, Zhang J, et al. Carbonaceous anode materials for non-aqueous sodium- and potassium-ion hybrid capacitors. *ACS Energy Letters*, 2021, 6(11): 4127–4154